Nanoscale

PAPER

View Article Online
View Journal | View Issue

Cite this: *Nanoscale*, 2016, **8**, 7119

Hybrid plasmonic gap modes in metal film-coupled dimers and their physical origins revealed by polarization resolved dark field spectroscopy†

Guang-Can Li, Yong-Liang Zhang and Dang Yuan Lei*

Received 29th December 2015,
Accepted 26th February 2016

DOI: 10.1039/c5nr09260d

www.rsc.org/nanoscale

Plasmonic gap modes sustained by metal film-coupled nanostructures have recently attracted extensive research attention due to flexible control over their spectral response and significantly enhanced field intensities at the particle–film junction. In this work, by adopting an improved dark field spectroscopy methodology – polarization resolved spectral decomposition and colour decoding – we are able to "visualize" and distinguish unambiguously the spectral and far field radiation properties of the complex plasmonic gap modes in metal film-coupled nanosphere monomers and dimers. Together with full-wave numerical simulation results, it is found that while the monomer–film system supports two hybridized dipole-like plasmon modes having different oscillating orientations and resonance strengths, the scattering spectrum of the dimer–film system features two additional peaks, one strong yet narrow resonant mode corresponding to a bonding dipolar moment and one hybridized higher order resonant mode, both polarized along the dimer axis. In particular, we demonstrate that the polarization dependent scattering radiation of the film-coupled nanosphere dimer can be used to optically distinguish from monomers and concurrently determine the spatial orientation of the dimer with significantly improved accuracy at the single-particle level, illustrating a simple yet highly sensitive plasmon resonance based nanometrology method.

Introduction

Resonant plasmonic nanostructures have attracted substantial attention in recent years and are used for a variety of photonic and biomedical applications because they support localized surface plasmon resonances (LSPRs) that can confine light in a deep subwavelength volume and strongly enhance the near field strength. As a result, light can be strongly absorbed and scattered by plasmonic nanoparticles, making them a novel type of contrast agent for biomedical imaging.[1,2] For instance, the strong absorption of plasmonic nanoparticles enables efficient generation of local resistive heating that can be exploited in photothermal therapy for cancer treatment and thermal acoustic imaging.[3,4] On the other hand, the enhanced near-field intensities in the vicinity of the metallic nanostructures upon excitation of their surface plasmon resonances can be utilized not only to amplify various linear optical effects, including surface plasmon-enhanced photoluminescence and fluorescence,[5–10] and surface enhanced Raman scattering (SERS),[11–14] but also to promote many kinds of nonlinear optical processes, including second/third harmonic generation (S/THG)[15–17] and two-photon absorption induced luminescence (TPL),[18–20] both occurring in metal nanostructures themselves and metal–semiconductor hybrids.

In general, the plasmonic modes as well as the optical response of the plasmonic nanostructures are strongly dependent on the geometry, symmetry and topology of the constitutive elements. To realize the desired optical properties for specific applications,[21–26] considerable efforts have been made to design, fabricate and characterize various metal nanostructures by rational assembling of two or more individual nanoparticles into single entities to create new plasmon resonances. In such complex structures, coupled LSPRs arise due to the strong near field coupling between the constitutive elements. Typical examples include the bonding and antibonding plasmons in a metal nanoparticle dimer,[27,28] superradiant and subradiant plasmons[29,30] and plasmonic Fano resonances[31,32] in metal nanoparticle oligomers. Two elegant theoretical tools – plasmon hybridization[33] and transformation optics[34,35] – have provided deep physical insights into the occurrence of new plasmon resonances in some of the aforementioned coupled nanostructures. In close analogy to the strong interaction between a fluorescent molecule and a neigh-

---

Department of Applied Physics, The Hong Kong Polytechnic University, Hong Kong, China. E-mail: dylei@polyu.edu.hk

†Electronic supplementary information (ESI) available. See DOI: 10.1039/c5nr09260d

bouring metal film, the system of metal film-coupled nanoparticles has recently received a great deal of research attention.[36–44] In this system, the presence of the underlying metallic film breaks the rotational symmetry of spherical nanoparticles, resulting in a strong coupling between the plasmon mode supported by the individual nanoparticle with its induced image on the film. As a result, the nanogaps between the particles and the film behave like hot spots with an extremely large field concentration which promise many plasmon-mediated optical sensing and enhancement applications.[45–47] Moreover, this film-coupled nanoparticle system offers a versatile platform for exploring a variety of fundamental nanophotonic phenomena such as spatial nonlocality[48] and quantum tunnelling when the gap is less than 0.5 nm.[49] Thus far, most previous investigations have been focused primarily on the system consisting of a single nanoparticle atop a metal film.[50–53] In the monomer–film system, the interaction between the dipolar plasmon mode sustained by the nanoparticle and the underlying film, as well as the tuning mechanism of the plasmon mode through gap distance controlling are extensively studied. However, little light has been shed on the effect of the underlying metal film on the coupling plasmon modes sustained by complex nanostructures sitting above. Thus, there is very little knowledge about plasmonic properties (resonance position and radiation behaviour) of metal film-coupled nanoparticle clusters like dimers or more complex nanostructures and the potential applications associated with these interesting systems also remain unexplored.[54–56]

In the present work, we report for the first time on the experimental investigation of the coupled LSPRs in a metallic film-coupled dimer system. By using the improved dark field spectroscopy methodology based on polarization resolved spectral decomposition and colour decoding, we “visualize” and distinguish the spectral and radiation properties of the complex plasmonic gap modes in gold film-coupled nanosphere monomers and dimers with nanometric particle–film and particle–particle gap distances. It is found that both monomer– and dimer–film nanostructures support two hybridized dipolar plasmon modes at 550 and 830 nm, both with distinctively different scattering intensities and spectral linewidths. The far-field radiation pattern of the former (latter) mode is featured with a green solid spot (red doughnut shape), indicating the excitation of an in-plane (out-of-plane) dipole moment that is consistent with full-wave simulation results. More interestingly, due to more structural degrees of freedom, the dimer–film structure shows two additional narrow-linewidth scattering peaks at 530 and 660 nm, corresponding to a higher order mode and a bonding dipolar mode, respectively, both with scattering intensities highly dependent on the in-plane polarization direction relative to the dimer orientation. In particular, we demonstrate that the observed in-plane polarization sensitive gap modes of the film-coupled dimer constitute a new plasmonic nanometrology tool that can be used to precisely resolve the spatial orientation of the dimer and also optically distinguish dimers from monomers.

Experimental and numerical sections

Sample preparation

A gold film was prepared on an ultra-clean coverslip (Schott Nexterion, Germany) using a thermal evaporator (Nexdep, Angstrom Engineering, Inc.). The thickness and surface roughness (RMS) of the gold film are about 45 nm and 0.5 nm both determined by AFM measurements (Nanoscope V, Veeco). Water-diluted monodisperse gold nanospheres of diameter 100 ± 8 nm (NanoSeeds, Inc., Hong Kong) were drop-cast on the gold film and left to dry in air for seconds to form gold-film coupled nanosphere monomers and dimers.

Optical characterization

Optical microscopy and spectroscopy were performed with an Olympus BX-51 upright microscope equipped with a standard dark-field optical module using a 100× dark-field objective (LMPlan, Olympus). Two sets of illumination configurations were used for un-polarized and polarized excitations, respectively. A standard un-polarized illumination configuration comes with the microscope itself while a home-made optical module allows for polarization controlled oblique illumination. Dark-field images and the spectra of individual nanostructures were recorded respectively using a colour CCD camera (QICAM 12-bit, QImaging, Inc.) and an imaging spectrometer (Acton SP2300) equipped with a grey CCD camera (PIXIS:400BR eXcelon). Colour decoding of the dark-field images was carried out using the Matlab software with which false-colour images (blue, green and red) were extracted from the three colour channels of the captured true-colour dark-field images.

Electrodynamics simulations

Distributions of the surface charge density for the film-coupled Au nano-particles were numerically calculated using a commercially available FEM package (COMSOL Multiphysics 4.3a with RF module). When performing the full wave simulation of the coupled system, the scattering field was calculated with a standard two-step process in which the background field is first computed for the same geometry in the absence of the particles under s- or p-polarized illumination with an incidence angle of 70° from the surface normal. Here, the surface charge density is characterized by the normal component of the electric field. In all calculations, the frequency dependent permittivity of Au was modelled using the experimental data of Johnson and Christy with linear interpolation.[57] The glass substrate was modelled using a constant refractive index of 1.5. To simplify the simulations, we have neglected the polymer surrounding the Au spheres. In order to simulate the infinite air and substrate region, the computation domain was truncated by perfect matched layers (PMLs) to reduce reflections. The simulation domain is finely meshed with the smallest size of 0.25 nm in the gap region so that the convergence of the results and the accuracy of the computed fields are confirmed.

Results and discussion

Morphological and optical characterization of film-coupled nanoparticles

To generate the plasmonic nanostructures supporting gap plasmon resonances, gold nanospheres of 100 nm diameter were deposited from a colloidal solution onto a bare gold film of 45 nm thickness. Due to the presence of a surfactant polymer coating – cetyltrimethylammonium bromide (CTAB) – on the gold nanospheres, an estimated gap distance of about 1 nm is formed at the nanosphere–film junctions while a gap distance of 2 nm at the nanosphere–dimer junction. Fig. 1a depicts a schematic of the gold film-coupled nanospheres and two different dark-field illumination configurations used in our experiment. The left panel shows an un-polarized illumination scheme with a commercial dark-field microscope system. Although a linear polarizer can be inserted in the light path before the objective, the polarization direction of the incident annular beam cannot be well defined with respect to the nanostructure orientation, particularly for the nanoparticle dimer. To overcome this limitation, we have constructed an illumination arm with which the incident polarization can be continuously tuned from s- to p-polarized as shown in the right panel of Fig. 1a as well as in Fig. 2a.[44] In addition, the incident angle can also be tuned within a finite range beyond the solid angle defined by the numerical aperture of the objective. This improvement has enabled polarization-selective and angle-dependent excitation of individual plasmon resonance modes in complex metallic nanostructures, significantly facilitating the understanding of their mode characteristics.

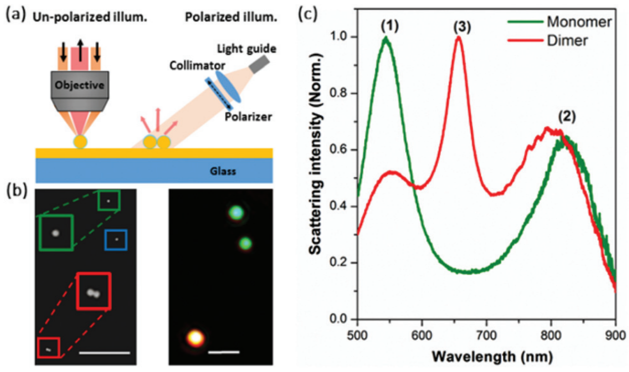

Fig. 1 (a) Schematic of gold film-coupled nanosphere monomers and dimers under standard un-polarized (left) and home-built polarized (right) excitation configurations. The thin, light-blue shells represent the CTAB coatings on gold nanospheres. (b) SEM micrograph (left) of two nanosphere monomers (enclosed by the green and blue squares) and a nanosphere dimer (enclosed by the red square) both dispersed on a 45 nm thick gold film. The right panel shows the corresponding optical dark-field image for the same sample area. The scale bars in both images are 2 μm. The bigger green and red squares in the SEM image show an enlarged view of the monomer and dimer structures, respectively, with their scattering spectra shown in (c) under an un-polarized illumination (green for monomer and red for dimer).

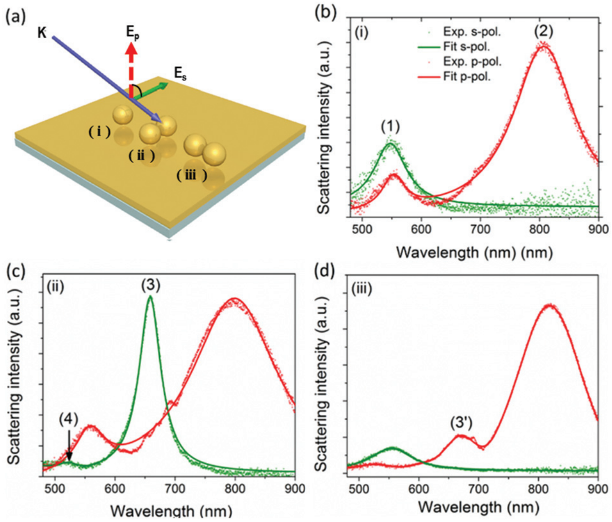

Fig. 2 (a) Schematic of the s- (green solid arrow) and p- (red dashed arrow) polarized incidence configurations for illuminating the single nanosphere monomer and the two orthogonally orientated nanosphere dimers. (b–d) Recorded scattering spectra (dots) for the three cases (i–iii) under the s- and p-polarized illuminations as shown in (a) and their fits with single or multiple Lorentz oscillators (lines).

Fig. 1b shows the pattern-matched scanning electron microscopy (SEM, left panel) and true-colour optical microscopy (right panel) images for a typical area of the sample used in our study, with the latter captured under an un-polarized dark-field illumination with an Olympus BX-51 microscope. Three single nanostructures, including one nanosphere dimer and two monomers, can be clearly seen in the observation window of both images. In the dark-field image, the two gold film-coupled monomers show strong scattering in the green region while the nanosphere dimer efficiently scatters the red light with intensity saturation, consistent with the recorded scattering spectra as shown in Fig. 1c. The scattering spectrum of the monomer structure exhibits two peaks at wavelengths ~550 and 830 nm, labelled as modes (1) and (2), respectively. In addition to the two scattering peaks occurring at similar spectral positions as that in the monomer case, the dimer structure exhibits an additional peak at ~660 nm labelled as mode (3), which has a much stronger scattering intensity yet narrower spectral linewidth (FWHM: 44 nm) than the other two peaks (see also Fig. S1 in the ESI†). As shown in the following, the mode nature of the three scattering peaks observed in both film-coupled nanostructures will be investigated in great detail by combining polarization-resolved far-field scattering measurements with full-wave electromagnetic simulations of surface charge distributions at the resonant wavelengths.

Polarization-resolved spectral decomposition of complex plasmonic gap modes

To reveal the physical origins for the observed plasmonic modes, we performed polarization-resolved scattering measurements for both film-coupled monomers and dimers with the polarized illumination configuration shown in Fig. 1a, which allows an elegant spectral decomposition of their un-polarized scattering spectra shown in Fig. 1c. Fig. 2a shows a schematic of the s- and p-polarized oblique incidences with respect to the two orthogonal orientations of the nanosphere dimer. Fig. 2b shows that the scattering spectrum of the film-coupled monomer structure (case (i) in Fig. 2a) recorded under the s-polarized illumination exhibits only one peak at a wavelength of ~550 nm, which is at the same spectral position as mode (1) labelled in Fig. 1c, indicating that this plasmon resonance mode only responds to horizontal polarization. The observed far-field excitation polarization dependence is further confirmed by the simulated near-field surface charge distribution for a geometrically simplified film-coupled monomer as shown in the first column of Fig. 3a and b, which reveal the excitation of a hybridized plasmon mode formed by the coupling between the quadrupole plasmon mode of the individual nanosphere monomer[58] and the dipolar plasmon mode induced in the metal film. While the dark quadrupole plasmon is a nonradiative mode, the far field radiation can only be attributed to the net dipole moment at the upper part of the nanosphere as a result of the radiation cancelling between the two anti-parallel oscillating charge pairs within the gap region. This simplifying of the hybridized plasmon mode to a net dipolar mode will also be validated afterwards by the far field radiation pattern with a solid point-spread function shape as illustrated in Fig. 4b. However, Fig. 3c shows that the near-field enhancement associated with the dark mode at the particle–film gap region is significantly larger than that induced by the weak dipolar mode at the upper part of the nanosphere. In sharp contrast, the scattering spectrum shown in Fig. 2b for the monomer under the p-polarized illumination is dominated by an intense peak at a wavelength of ~830 nm, similar to the spectral position of mode (2) labelled in Fig. 1c, and a relatively weak peak at ~550 nm, similar to mode (1) excited by the horizontal polarization component of the p-polarized beam. We can thus attribute the plasmon mode (2) to the excitation of a bonding dipolar mode consisting of a vertical dipole moment of the gold nanosphere and an induced one in the gold film, which is fully consistent with the surface charge distribution as shown in the second column of Fig. 3a and b. The two plasmonic dipoles interfere constructively at the gap region and therefore produce strong far-field radiation to free space as well as significantly enhanced near-field strength as can be seen from Fig. 3c. This way the plasmonic response of the gold film-coupled nanosphere monomer is completely decomposed in the far-field regime and fully interpreted from a perspective of the electric near-field interaction.

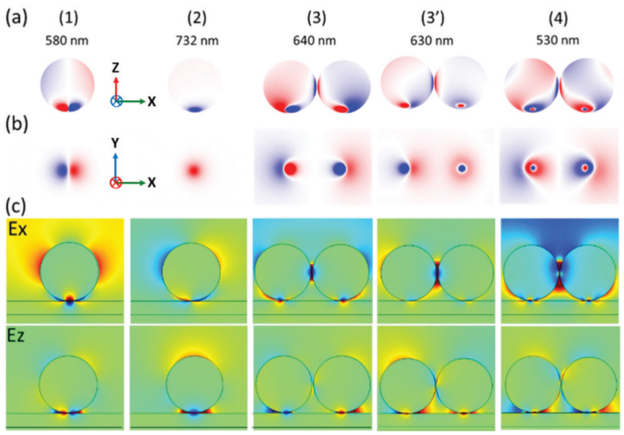

Fig. 3 (a and b) Surface charge distribution profiles computed for the geometrically simplified gold film-coupled nanosphere monomer (first and second panels) and dimer (third to fifth panels). For simplicity, the CTAB coating on the gold nanosphere is not considered in simulations. To have a better visualization of the particle–film gap region, the charge distribution profiles are separately shown in two views, a tilted view for the nanospheres (a) and a top view for the film (b). (c) Incidence-plane distribution of the *x* and *z* electric near-field components in the structures in (a and b) at the same wavelengths.

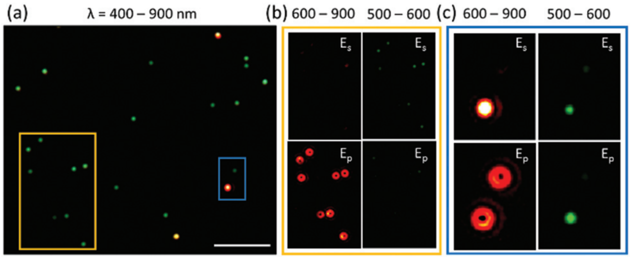

Fig. 4 (a) True-colour dark-field image of gold nanosphere monomers and dimers dispersed on a gold film and the squared areas are of our interest. The scale bar is 5 μm. (b) False-colour images of the area enclosed by the yellow square in (a) captured with the red (left column) and green colour channels (right column) under the s- and p-polarized illuminations, respectively. (c) Enlarged false-colour images of the area enclosed by the blue square in (a), including a monomer (upper) and a dimer (lower) both captured and illuminated under the same conditions as (b).

We then turn to the two cases of the gold film-coupled nanosphere dimer. Under the s-polarized illumination, Fig. 2c shows that the scattering spectrum for the dimer in case (ii) is dominated by an intense peak at a wavelength of ~660 nm, the same spectral position as mode (3) in Fig. 1c, accompanied by a much weaker peak at ~530 nm labelled as mode (4) (further evidenced in ESI Fig. S2†). In addition, these two peaks disappear under the p-polarized excitation, suggesting that they respond only to horizontal polarization. The simulated surface charge distribution for the plasmon mode (3) shown in the third column of Fig. 3a and b demonstrates that each nanosphere–film gap supports two anti-parallel horizontal dipole moments, leading to dipolar cancellation in the same manner as the plasmon mode (1) in the monomer structure and thus negligible contribution to the far-field scattering. However, at the gap between the two nanospheres, the charge distribution reveals a bonding dipole moment, which can effectively radiate energy to free space and thus give rise to the strong scattering peak at ~660 nm. The fifth column of Fig. 3a and b shows that the new plasmon mode (4) is a higher order resonance as can be seen from the distorted surface charge distribution both at the two nanospheres and the underlying film. Different from the plasmon modes (1) and (2), the electric near-field strength is the strongest at the gap volume between the two nanospheres for the plasmon modes (3) and (4) simply because the incident polarization is along the long axis of the dimer. A completely different scenario emerges for the p-polarized illumination: the scattering spectrum for the same dimer has two peaks at the same spectral positions as the plasmon modes (1) and (2), which can be attributed to the respective excitation of a horizontally antibonding and a vertically bonding dipole moment in each particle–film gap. Because the incident polarization is perpendicular to the long axis of the dimer, the electromagnetic coupling between the two nanospheres is negligible and therefore the positions of the two scattering peaks are very close to that observed for the monomer structure.

Fig. 2d shows the scattering spectra recorded for the dimer in case (iii). Since the long axis of the dimer is within the p-polarized incidence plane such that the s-polarized illumination cannot induce strong plasmonic coupling between the two nanospheres and thereby gives rise to only one weak scattering peak at the same spectral position as the plasmon mode (1) in the monomer system. Under the p-polarized illumination, the scattering spectrum shows three distinctive peaks, with the first one at ~830 nm corresponding to the plasmon mode (2), the second at ~530 nm to the plasmon mode (4) and the third at ~670 nm (a redshift of ~10 nm compared to the plasmon mode (3)) labelled as mode (3′). In fact, this new plasmon mode (3′) is a hybridized resonance between the plasmon modes of (2) and (3) because its surface charge distribution inherits all main features from both modes as can be seen from the fourth panels of Fig. 3a and b. As a result, Fig. 3c shows that the plasmonic near field for this mode is significantly enhanced both at the particle–film and particle–particle gaps.

Polarization-resolved colour decoding of dark-field scattering radiation patterns

To gain further insights into the correlation between the simulated near field origination and the far field characteristic of each plasmon mode of the metal film coupled nanosphere monomer and dimer, we also strive to filter out the far field scattering pattern of each plasmon resonance mode. However, the dark-field image captured for a plasmonic nanostructure with a standard microscopy system is a simple superposition of different colours, making it difficult to resolve the radiation pattern of a specific plasmon mode of interest and consequently losing important information on its physical nature.[59] To resolve this issue associated with the standard microscopy system, here we develop a polarization resolved colour decoding method to better "visualize" the radiation pattern for each plasmon mode using the three colour channels (blue, green and red) built in a CCD camera. This is realized due to the fact that the plasmonic gap modes observed for the gold film-coupled monomer and dimer are well separated in the spectrum and can be selectively excited by choosing appropriate incident polarization. Therefore, we can combine polarization controlled excitation and colour decoding to filter out the far field radiation pattern for each plasmon mode.

Fig. 4a shows a true-colour dark-field image captured for a sample area under the un-polarized illumination, and the image is dominated by green and red colours due to the relatively strong scattering peaks at 550 and 660 nm, corresponding to the modes (1) and (3). The green spots enclosed in the yellow square of the image are nanosphere monomers while the green and red spots enclosed in the blue square are a monomer and a dimer, respectively. Using the polarization-resolved colour decoding method, on the one hand, the radiation pattern of the scattering peak at 550 nm for the monomers can be imaged with the green channel (effective collection band: 500–600 nm) of the CCD camera combined with the s-polarized incidence (termed as G-S combination). The upper-right panel of Fig. 4b shows the false-colour image captured for the area enclosed by the yellow square in Fig. 4a with the G-S combination, and the image clearly resolves a solid spot pattern for each nanoparticle, arising from the far-field radiation by the induced horizontal dipole moment as shown in the first column of Fig. 3. The lower-right panel shows that the image of the same sample area captured with a G-P collection–excitation combination (green-channel collection combined with p-polarized illumination) appears much darker because of a significantly smaller horizontal field component in the p-polarized illumination. On the other hand, the radiation pattern of the scattering peak at 830 nm for the monomers can be clearly imaged with a R-P collection–excitation combination (red-channel collection combined with p-polarized illumination), with the image shown in the lower-left panel exhibiting a doughnut shape due to the excitation of a vertically aligned dipole moment as revealed in the second column of Fig. 3. The image captured for the same sample with an R-S collection–excitation combination (red-channel collection combined with s-polarized illumination) appears nearly dark as can be seen in the upper-left panel of Fig. 4. This way we have directly decoded the scattering colours for the two distinctive plasmon modes (1) and (2) for the gold film-coupled monomers and clearly resolved their respective far-field radiation patterns that are often hidden in the dark-field image captured concurrently with all three channels of a CCD camera for the same sample under an un-polarized illumination. This approach can also be applied to far field scattering characterization of other complex nanostructures.

More interesting observations can be made when comparing the decoded radiation patterns of the gold film-coupled monomer and dimer (ii) enclosed in the blue square in Fig. 4a. The upper- and lower-right panels of Fig. 4c render the false-colour images captured for the two nanostructures with the G-S and G-P collection–excitation combinations, respectively. Different from the monomer structure that is manifested as a blurred solid spot (corresponding to mode (1)) under both polarized illuminations, the dimer structure exhibits a bright solid spot radiation pattern simply due to the scattering peak at 530 nm under the s-polarized illumination, corresponding to mode (4), and the collective scattering contribution at 550 nm from the two nanospheres under the p-polarized illumination, corresponding to mode (1). This image contrast provides an easy and effective approach to distinguish nanoparticle monomers and dimers in the same sample area. The false-colour image captured for both nanostructures with the R-P combination shows a nearly perfect doughnut shape as can be seen in the lower-left panel, both corresponding to mode (2) arising from the induced bonding dipolar moment at each particle–film gap. The image captured with the R-S combination shows a solid radiation spot for the dimer structure, corresponding to its mode (3) at 660 nm, and no signal for the monomer structure. Although the modes (2) and (3) for the dimer structure are imaged with the same red channel, the combination with the selective polarization has enabled separate visualization of their radiation patterns.

Single-particle plasmonic nanometrology of nanoparticle dimer orientation

Since the far-field scattering response of the gold film-coupled nanosphere dimer is extremely sensitive to spatial orientation of the dimer relative to incident polarization, we propose a polarization-resolved nanometrology spectroscopy method, combining the above-discussed colour decoding method, to determine the dimer orientation at the single nanostructure level. In particular, the hybrid plasmon mode (3) essentially originates from a bonding dipole moment oscillating along the long axis of the nanosphere dimer, leading to its far-field radiation polarized along the same direction. By monitoring the scattering intensity at the resonant wavelength of this plasmon mode as a function of detection polarization (corresponding to the transmission axis of an analyser placed right before the detector), the accurate orientation of the dimer can be determined.

Fig. 5a shows the pattern-matched dark-field (dashed-yellow square enclosed area) and SEM images of two gold film-coupled nanosphere dimers with different orientations. While the spatial alignment of the two nanosphere dimers can be well resolved in the SEM image, it cannot be distinguished in the dark-field image captured under un-polarized illumination though the scattering colours exhibit a slight difference for the two nanostructures. Fig. 5b shows a series of false-colour dark-field images captured with the red and green channels as a function of detection polarization. In the red-channel images, the two dimers show maximum (minimum) intensities at the analyser angle parallel (perpendicular) to their own dimer axis. This polarization dependence of the scattering intensity allows for qualitative determination of the dimer orientation. The images captured with the green channel, however, show no significant intensity variation with the detection polarization for both dimers at all polarization angles as can be seen from the right panel of Fig. 5b. To achieve quantitative determination of the dimer orientation, Fig. 5c shows the detection–polarization dependent scattering intensity integrated within the red colour channel for both nanosphere dimers, and the polar plots exhibit maximum at a polarization angle of ~15° for the upper-right dimer and ~135° for the lower-left one, in good agreement with the SEM characterization. Due to the strong radiation and polarization sensitivity of the plasmon mode (3), this proposed nanometrology is advanced with a significantly improved signal-to-noise ratio yet simplicity in measurement configuration.[60,61]

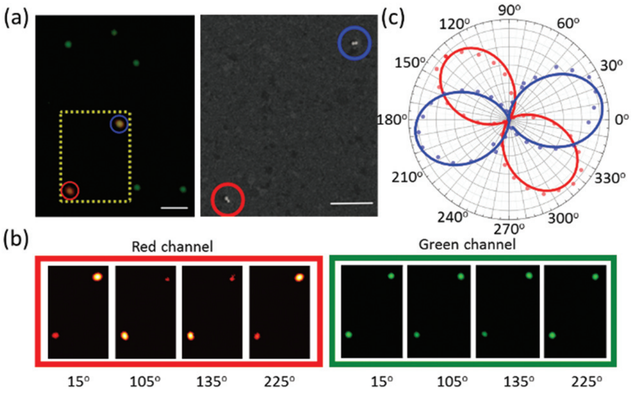

Fig. 5 Determination of the spatial orientation of a metal film-coupled nanosphere dimer using polarization resolved colour decoding combined with plasmon resonance based nanometrology. (a) Pattern-matched dark-field (left) and SEM (right) images for gold film-coupled nanospheres. Two nanosphere dimers are enclosed in a dashed-yellow square in the dark-field image, with their corresponding SEM image shown in the right panel exhibiting different spatial orientations. (b) The false-colour images of the two dimers in (a) captured with the red (left) and green (right) channels as a function of detection polarization defined with respect to horizontal. (c) Polar plot of the scattering intensity (dots) integrated within the red colour channel of the CCD camera for the two dimers shown in (a). The solid lines are cosine-square fits to the measured data.

Conclusions

In summary, we have thoroughly revealed the complex plasmonic gap modes sustained by gold film-coupled nanosphere monomers and dimers at the single particle level using a polarization-resolved spectral decomposition and colour decoding method. Together with the full-wave electrodynamic simulation results, this method uncovers that the film-coupled monomer supports two plasmonic modes, one with a weak dipole moment aligned in the horizontal direction and the other one with two bonding dipole moments in the vertical direction. In addition to these two plasmon modes, the film-coupled dimer sustains the other two resonance modes, one with two distorted bonding dipole moments along the dimer axis and the other one with strong high-order features. Based on the polarization dependent far-field scattering response, we have proposed a plasmonic nanometrology tool that has been successfully applied to determine the spatial orientation of plasmonic nanosphere dimers with a significantly improved signal to noise ratio and can be extended to resolve the spatial arrangement of plasmonic nanoclusters in general. We believe that our systematic study of the metal film-coupled monomers and dimers will pave the way for further revealing the mechanism of the electromagnetic interaction between more complex nanostructures and metal films.

Acknowledgements

We acknowledge the financial support by the Hong Kong Polytechnic University (Grant No. 1-ZE23) and the Hong Kong Research Grants Council (ECS Grant No. 509513).

References

1 C. Loo, A. Lowery, N. Halas, J. West and R. Drezek, *Nano Lett.*, 2005, **5**, 709–711.
2 X. Huang, I. H. El-Sayed, W. Qian and M. A. El-Sayed, *J. Am. Chem. Soc.*, 2006, **128**, 2115–2120.
3 S. Egerev, S. Ermilov, O. Ovchinnikov, A. Fokin, D. Guzatov, V. Klimov, A. Kanavin and A. Oraevsky, *Appl. Opt.*, 2009, **48**, C38–C45.
4 S. Mallidi, T. Larson, J. Tam, P. P. Joshi, A. Karpiouk, K. Sokolov and S. Emelianov, *Nano Lett.*, 2009, **9**, 2825–2831.
5 W. Rao, Q. Li, Y. Wang, T. Li and L. Wu, *ACS Nano*, 2015, **9**, 2783–2791.
6 L. Jiang, T. Yin, Z. Dong, H. Hu, M. Liao, D. Allioux, S. J. Tan, X. M. Goh, X. Li, J. K. W. Yang and Z. Shen, *ACS Photonics*, 2015, **2**, 1217–1223.
7 D. Huang, C. P. Byers, L. Wang, A. Hoggard, B. Hoener, S. Dominguez-Medina, S. Chen, W. Chang, C. F. Landes and S. Link, *ACS Nano*, 2015, **9**, 7072–7079.
8 Z.-K. Zhou, D. Y. Lei, J. Liu, X. Liu, J. Xue, Q. Zhu, H. Chen, T. Liu, Y. Li, H. Zhang and X. Wang, *Adv. Opt. Mater.*, 2014, **2**, 56–64.
9 D. Y. Lei and H. C. Ong, *Appl. Phys. Lett.*, 2007, **91**, 2005–2008.
10 D. Y. Lei, J. Li and H. C. Ong, *Appl. Phys. Lett.*, 2007, **91**, 21112.
11 K. Kneipp, Y. Wang, H. Kneipp, L. T. Perelman, I. Itzkan, R. R. Dasari and M. S. Feld, *Phys. Rev. Lett.*, 1997, **78**, 1667–1670.
12 S. Nie, *Science*, 1997, **275**, 1102–1106.
13 D.-K. Lim, K.-S. Jeon, H. M. Kim, J.-M. Nam and Y. D. Suh, *Nat. Mater.*, 2010, **9**, 60–67.
14 X. Zhang, Y. Zheng, X. Liu, W. Lu, J. Dai, D. Y. Lei and D. R. MacFarlane, *Adv. Mater.*, 2015, **27**, 1090–1096.
15 J. Butet, J. Duboisset, G. Bachelier, I. Russier-Antoine, E. Benichou, C. Jonin and P. F. Brevet, *Nano Lett.*, 2010, **10**, 1717–1721.
16 A. Slablab, L. Le Xuan, M. Zielinski, Y. de Wilde, V. Jacques, D. Chauvat and J.-F. Roch, *Opt. Express*, 2012, **20**, 220.
17 M. Celebrano, X. Wu, M. Baselli, S. Großmann, P. Biagioni, A. Locatelli, C. De Angelis, G. Cerullo, R. Osellame, B. Hecht, L. Duò, F. Ciccacci and M. Finazzi, *Nat. Nanotechnol.*, 2015, **10**, 412–417.
18 R. a. Farrer, F. L. Butterfield, V. W. Chen and J. T. Fourkas, *Nano Lett.*, 2005, **5**, 1139–1142.
19 H.-D. Deng, G.-C. Li, Q.-F. Dai, M. Ouyang, S. Lan, V. a. Trofimov and T. M. Lysak, *Nanotechnology*, 2013, **24**, 075201.
20 Z. Guan, N. Gao, X. F. Jiang, P. Yuan, F. Han and Q. H. Xu, *J. Am. Chem. Soc.*, 2013, **135**, 7272–7277.
21 A. Aubry, D. Y. Lei, A. I. Fernández-Domínguez, Y. Sonnefraud, S. A. Maier and J. B. Pendry, *Nano Lett.*, 2010, **10**, 2574–2579.
22 D. Y. Lei, A. Aubry, S. A. Maier and J. B. Pendry, *New J. Phys.*, 2010, **12**, 093030.
23 X. Yu, D. Y. Lei, F. Amin, R. Hartmann, G. P. Acuna, A. Guerrero-Martínez, S. A. Maier, P. Tinnefeld, S. Carregal-Romero and W. J. Parak, *Nano Today*, 2013, **8**, 480–493.
24 C. L. Haynes and R. P. Van Duyne, *J. Phys. Chem. B*, 2001, **105**, 5599–5611.
25 C. L. Nehl, H. Liao and J. H. Hafner, *Nano Lett.*, 2006, **6**, 683–688.
26 C. Ruan, G. Eres, W. Wang, Z. Zhang and B. Gu, *Langmuir*, 2007, **23**, 5757–5760.
27 A. L. Koh, K. Bao, I. Khan, W. E. Smith, G. Kothleitner, P. Nordlander, S. A. Maier and D. W. McComb, *ACS Nano*, 2009, **3**, 3015–3022.
28 C. Y. Tsai, J. W. Lin, C. Y. Wu, P. T. Lin, T. W. Lu and P. T. Lee, *Nano Lett.*, 2012, **12**, 1648–1654.
29 Y. Sonnefraud, N. Verellen, H. Sobhani, G. A. E. Vandenbosch, V. V. Moshchalkov, P. Van Dorpe, P. Nordlander and S. A. Maier, *ACS Nano*, 2010, **4**, 1664–1670.
30 C.-Y. Chen, I.-W. Un, N.-H. Tai and T.-J. Yen, *Opt. Express*, 2009, **17**, 15372–15380.
31 B. Luk'yanchuk, N. I. Zheludev, S. A. Maier, N. J. Halas, P. Nordlander, H. Giessen and C. T. Chong, *Nat. Mater.*, 2010, **9**, 707–715.
32 M. Rahmani, D. Y. Lei, V. Giannini, B. Lukiyanchuk, M. Ranjbar, T. Y. F. Liew, M. Hong and S. A. Maier, *Nano Lett.*, 2012, **12**, 2101–2106.
33 E. Prodan, C. Radloff, N. J. Halas and P. Nordlander, *Science*, 2003, **302**, 419–422.
34 A. Aubry, D. Y. Lei, S. A. Maier and J. B. Pendry, *Phys. Rev. Lett.*, 2010, **105**, 2–5.
35 A. Aubry, D. Y. Lei, S. A. Maier and J. B. Pendry, *ACS Nano*, 2011, **5**, 3293–3308.
36 J. J. Mock, R. T. Hill, A. Degiron, S. Zauscher, A. Chilkoti and D. R. Smith, *Nano Lett.*, 2008, **8**, 2245–2252.
37 C. Lumdee, B. Yun and P. G. Kik, *Nanoscale*, 2015, **7**, 4250–4255.
38 S. Mubeen, S. Zhang, N. Kim, S. Lee, S. Krämer, H. Xu and M. Moskovits, *Nano Lett.*, 2012, **12**, 2088–2094.
39 B. Yu, J. Woo, M. Kong and D. M. O'Carroll, *Nanoscale*, 2015, **7**, 13196–13206.
40 F. Schertz, M. Schmelzeisen, R. Mohammadi, M. Kreiter, H. J. Elmers and G. Schönhense, *Nano Lett.*, 2012, **12**, 1885–1890.

41 J. J. Mock, R. T. Hill, Y. J. Tsai, A. Chilkoti and D. R. Smith, *Nano Lett.*, 2012, **12**, 1757–1764.

42 J. W. Ha, K. Marchuk and N. Fang, *Nano Lett.*, 2012, **12**, 4282–4288.

43 J. B. Lassiter, F. McGuire, J. J. Mock, C. Ciracì, R. T. Hill, B. J. Wiley, A. Chilkoti and D. R. Smith, *Nano Lett.*, 2013, **13**, 5866–5872.

44 D. Y. Lei, A. I. Fernández-Domínguez, Y. Sonnefraud, K. Appavoo, R. F. Haglund, J. B. Pendry and S. A. Maier, *ACS Nano*, 2012, **6**, 1380–1386.

45 R. T. Hill, J. J. Mock, A. Hucknall, S. D. Wolter, N. M. Jokerst, D. R. Smith and A. Chilkoti, *ACS Nano*, 2012, **6**, 9237–9246.

46 L. Du, D. Y. Lei, G. Yuan, H. Fang, X. Zhang, Q. Wang, D. Tang, C. Min, S. A. Maier and X. Yuan, *Sci. Rep.*, 2013, **3**, 3064.

47 D. O. Sigle, J. Mertens, L. O. Herrmann, R. W. Bowman, S. Ithurria, B. Dubertret, Y. Shi, H. Y. Yang, C. Tserkezis, J. Aizpurua and J. J. Baumberg, *ACS Nano*, 2015, **9**, 825–830.

48 C. Ciraci, R. T. Hill, J. J. Mock, Y. Urzhumov, a. I. Fernandez-Dominguez, S. A. Maier, J. B. Pendry, A. Chilkoti and D. R. Smith, *Science*, 2012, **337**, 1072–1074.

49 G. Hajisalem, M. S. Nezami and R. Gordon, *Nano Lett.*, 2014, **14**, 6651–6654.

50 X. Chen, Y. Yang, Y.-H. Chen, M. Qiu, R. J. Blaikie and B. Ding, *J. Phys. Chem. C*, 2015, **119**, 18627–18634.

51 B. de Nijs, R. Bowman, L. O. Herrmann, F. Benz, S. J. Barrow, D. O. Sigle, J. Mertens, A. Eiden, A. Ferrari, P. O. Scherman and J. J. Baumberg, *Faraday Discuss.*, 2014, **178**, 185–193.

52 N. Yamamoto, S. Ohtani and F. J. García De Abajo, *Nano Lett.*, 2011, **11**, 91–95.

53 R. T. Hill, K. M. Kozek, A. Hucknall, D. R. Smith and A. Chilkoti, *ACS Photonics*, 2014, **1**, 974–984.

54 Y. Wang, Z. Li, K. Zhao, A. Sobhani, X. Zhu, Z. Fang and N. J. Halas, *Nanoscale*, 2013, **5**, 9897–9901.

55 H. Liu, J. Ng, S. B. Wang, Z. H. Hang, C. T. Chan and S. N. Zhu, *New J. Phys.*, 2011, **13**, 0–8.

56 X. Wang, M. Li, L. Meng, K. Lin, J. Feng, T. Huang, Z. Yang and B. Ren, *ACS Nano*, 2014, **8**, 528–536.

57 P. B. Johnson and R. W. Christy, *Phys. Rev. B: Solid State*, 1972, **6**, 4370–4379.

58 A. Sobhani, A. Manjavacas, Y. Cao, M. J. McClain, F. J. García de Abajo, P. Nordlander and N. J. Halas, *Nano Lett.*, 2015, **15**, 6946–6951.

59 C.-Z. Huang, M.-J. Wu and S.-Y. Chen, *J. Phys. Chem. C*, 2015, **119**, 13799–13806.

60 K. Marchuk and N. Fang, *Nano Lett.*, 2013, **13**, 5414–5419.

61 J. W. Ha, *Nanoscale*, 2015, **7**, 13159–13163.